

The Impact of Enhanced Iron Opacity on Massive Star Pulsations: Updated Instability Strips^{*}

Ehsan Moravveji¹†

¹*Institute of Astronomy, KU Leuven, Celestijnenlaan 200D, 3001 Leuven, Belgium*

Accepted 2015 September 25. Received 2015 September 6; in original form 2015 August 19

ABSTRACT

Recently, Bailey et al. (2015) made a direct measurement of the Iron opacity at the physical conditions of the solar tachocline. They found that the wavelength-integrated Iron opacity is roughly 75% higher than what the OP and OPAL models predict. Here, we compute new opacity tables with enhanced Iron and Nickel contributions to the Rosseland mean opacity by 75% each, and compute three dense MESA grids of evolutionary models for Galactic O- and B-type stars covering from 2.5 to 25 M_{\odot} from ZAMS until $T_{\text{eff}} = 10000$ K after the core hydrogen exhaustion. We carry out non-adiabatic mode stability analysis with GYRE, and update the extension of the instability strips of heat-driven p- and g-mode pulsators, and the hybrid pulsating SPB- β Cep stars. We compare the position of two confirmed late O-type β Cep and eight confirmed hybrid B-type pulsators with the new instability domains, and justify that $\sim 75\%$ enhancement, only in Iron opacity, is sufficient to consistently reproduce the observed position of these stars on the $\log T_{\text{eff}}$ versus $\log g$ plane. We propose that this improvement in opacities be incorporated in the input physics of new stellar models.

Key words: asteroseismology – opacity – stars: massive – stars: oscillations

1 INTRODUCTION

The stellar opacity is a key ingredient of our simplified 1D stellar structure, evolution and pulsations models; it determines the efficiency of radiative energy transfer, and controls the luminosity, hence lifespan of stars. Indeed, any improvement in our understanding of stellar opacities impacts the morphology of evolutionary tracks, the distribution of basic thermodynamical quantities (such as temperature, pressure and density) inside the models, and changes the theoretical pulsation frequencies. It also shifts the theoretical isochrones, and consequently the ages of stellar populations.

Recently, Bailey et al. (2015) conducted a direct measurement of the Iron opacity at the physical conditions resembling the solar tachocline ($T = 1.91 - 2.26 \times 10^6$ K, $n_e = 0.7 - 4 \times 10^{22}$ cm⁻³). Their comparison between the wavelength-dependent Fe opacity and those computed from the Opacity Project (OP, Seaton et al. 1994; Badnell et al. 2005) showed that the models underestimate Fe opacity by 30% to 400% (their Fig. 3a and 3c), leading to the fact that the mea-

sured Iron Rosseland mean opacity (see below) is $\beta_{\text{Fe}} \approx 1.75$ times larger than the OP models. Moreover, Nickel is the 2nd abundant Iron-group element in typical main sequence (MS) stars. The similarity of the atomic structures of Fe and Ni has already allowed OP and OPAL teams to construct Ni monochromatic opacities by scaling Fe opacities (Badnell et al. 2005; Iglesias 2015). This implies that the Ni monochromatic opacity could be underestimated by roughly the same factor ≈ 1.75 as measured for Fe. Thus, there is still enough room for improving Ni opacity. It is noteworthy that the recent revised OPAL (Iglesias 2015) opacities for Fe reasonably agrees with the OP ones and is still significantly below the measurements. The improvements provided by Bailey et al. prompts an update to the opacity tables before any further stellar evolutionary models are computed.

One of the direct implications of Fe opacity enhancement is its immediate influence on destabilizing low-order p- and high-order g-modes in β Cep and Slowly Pulsating B (SPB) stars, where the Iron-opacity peak at $\log T \simeq 5.2$ K is already known to be responsible for (Gautschy & Saio 1993; Dziembowski & Pamiatnykh 1993; Dziembowski et al. 1993). The height of this opacity peak depends directly on (a) the assumed mixture, i.e. the relative abundance of the Iron-group elements, Fe, Ni, Co, Cr, and Mn (Salmon et al. 2012), (b) the assumed metallicity (e.g. $Z = 0.014$ versus $Z = 0.020$),

^{*} To reproduce the results, all software, opacity tables and the new instability strips are freely available for download via <https://fys.kuleuven.be/ster/Projects/ASAMBA>.

† E-mail: Ehsan.Moravveji@ster.kuleuven.be

and (c) the contribution of each element to the net opacity $\kappa_{\text{net}}(\nu)$. Consequently, with the increasing role of Iron-group elements in the Rosseland mean opacity (Sect. 2), the number of excited p- and g-modes increases, in addition to their instability domains on the Kiel ($\log T_{\text{eff}}$ versus $\log g$) diagram. Most importantly, the overlapping region between the two instability strips – where the so-called hybrid pulsators lie – depends critically on the computations of Fe and Ni radiative opacities. In this paper, we prepare new opacity tables with different Fe and Ni contributions (Sect. 2), and employ them to compute three evolutionary grids (Sect. 3) and their corresponding instability strips of the upper HR diagram (Sect. 4). By incorporating the Iron opacity enhancement, we solve the discrepancy between the predicted instability domain of hybrid SPB- β Cephei pulsators and those of detected hybrid B pulsators (Sect. 5).

2 ENHANCED MONOCHROMATIC IRON OPACITY AND THE ROSSELAND MEAN

The radiative opacity contains contributions from electron scattering κ_{es} , bound-bound inter-shell $\Delta n \geq 0$ transitions κ_{bb} , bound-free transitions including photo-ionizations κ_{bf} , and free-free transitions κ_{ff} . For a given photon frequency ν , the combined monochromatic photon absorption cross section for any element i is designated by $\kappa^i(\nu)$, and is summed as follows

$$\kappa^i(\nu) = \beta_i \left(\kappa_{\text{bf}}^i + \kappa_{\text{ff}}^i + \kappa_{\text{bb}}^i \right) \left[1 - e^{-h\nu/K_{\text{B}}T} \right], \quad (1)$$

where K_{B} is the Boltzmann constant. The net frequency-dependent opacity $\kappa_{\text{net}}(\nu)$ is a sum over N available elements, i.e. $\kappa_{\text{net}}(\nu) = \kappa_{\text{es}} + \sum_{i=1}^N \kappa^i(\nu)$. The Rosseland mean opacity, here $\bar{\kappa}$, is a harmonic mean of the reciprocal opacity of stellar material weighted by the Planck energy distribution function $B(\nu, T)$ and integrated over frequency (or wavelength)

$$\frac{1}{\bar{\kappa}} = \frac{1}{dB/dT} \int_0^\infty \frac{1}{\kappa_{\text{net}}(\nu)} \frac{dB(\nu, T)}{dT} d\nu. \quad (2)$$

Note that $dB/dT = \int_0^\infty \nu d\nu dB(\nu, T)/dT = acT^3/\pi$ where a and c are the radiation constant and speed of light, respectively.

We introduced an additional vector of enhancement factors β_i in Eq. (1) that allows modifying the contributions of individual elements to the net opacity before carrying out the Rosseland mean in Eq. 2. Setting all factors to unity, $\beta_i=1$, reproduces the default monochromatic OP opacities. We choose to set $\beta_{\text{Fe}} = 1.75$ as suggested by Bailey et al. (2015), and compare the resulting Rosseland mean with the default case where $\beta_{\text{Fe}} = 1.0$. Additionally, we predict mode instability properties for the case $\beta_{\text{Ni}} = 1.75$.

The computation of monochromatic (Eq. 1) and the Rosseland mean (Eq. 2) opacities are possible by using the public `OPCD 3.3` (Seaton 2005; Badnell et al. 2005). Hu et al. (2010) have already implemented an interface to call `OPCD` from the MESA stellar structure and evolution code (Paxton et al. 2011, 2013, 2015) that we also use. Currently, `OPCD` uses atomic data for 17 elements (hence $i=\text{H, He, C, N, O, Ne, Na, Mg, Al, Si, S, Ar, Ca, Cr, Mn, Fe and Ni}$). We developed additional routines that call the `chem`, `eos` and `kap` modules in MESA to compute κ for any assumed β_i over a pre-defined range of temperatures and densities. The output

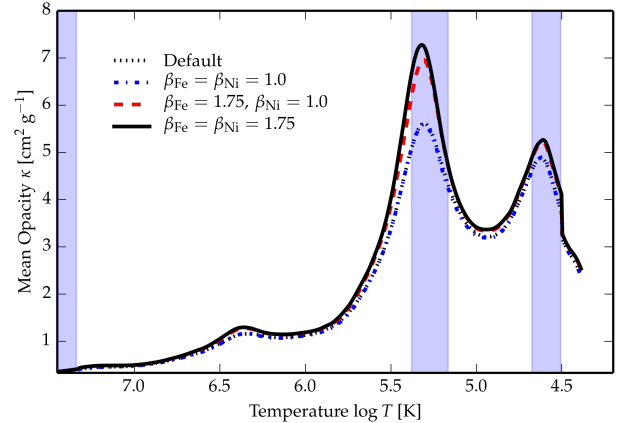


Figure 1. Rosseland opacity κ in a $10 M_{\odot}$ star at fixed center hydrogen mass fraction $X_{\text{c}} = 0.60$ and $Z = 0.014$. The profiles for the default MESA tables (black dotted) and $\beta_{\text{Fe}} = \beta_{\text{Ni}} = 1.0$ (blue dash-dot) are identical. The red dashed and black solid curves correspond to $(\beta_{\text{Fe}}, \beta_{\text{Ni}}) = (1.75, 1.0)$, and $(1.75, 1.75)$, respectively. The convective regions are highlighted in blue.

is a set of ASCII tables identical to the OPAL Type I tables which are commonly used for interpolation in 1D stellar evolution codes.

3 STELLAR MODELS

We computed new sets of opacity tables by adopting the Asplund et al. (2009) solar mixture for three combinations of $(\beta_{\text{Fe}}, \beta_{\text{Ni}}) = (1.0, 1.0)$, $(1.75, 1.0)$ and $(1.75, 1.75)$. Fig. 1 compares the resulting κ profiles using the default MESA OP opacity tables, and the new tables with $(\beta_{\text{Fe}}, \beta_{\text{Ni}}) = (1.0, 1.0)$, $(1.75, 1.0)$ and $(1.75, 1.75)$, respectively. The first two κ profiles are identical, demonstrating that our new $\beta_{\text{Fe}} = 1.0$ tables are consistent with the default MESA tables. By increasing Fe and Ni opacity factors $(\beta_{\text{Fe}}, \beta_{\text{Ni}})$ to $(1.75, 1.0)$ and $(1.75, 1.75)$, the height of the Iron-bump increases by $\sim 24\%$ and $\sim 30\%$, respectively. Similarly, the total photon interaction cross section, i.e. $\sigma^2 = \int_0^{M_{\star}} \kappa dm [\text{cm}^2]$ increases by 5.11% and 5.57%, respectively, when compared to the case of $(\beta_{\text{Fe}}, \beta_{\text{Ni}}) = (1.0, 1.0)$. Here, M_{\star} and dm are the total mass and mass increments.

Then, we plugged the new opacity tables into MESA to compute three evolutionary grids of 101 evolutionary tracks each, uniformly spaced between 2.5 and $25 M_{\odot}$ in logarithmic scale. We adopted the Galactic B-star composition of Nieva & Przybilla (2012) $(X_{\text{ini}}, Z_{\text{ini}}) = (0.71, 0.014)$, and the Asplund et al. (2009) mixture. We include mass loss to remain consistent with observation, although it has a stabilizing effect on heat-driven modes (Godart et al. 2009). An exponential core overshoot of $f_{\text{ov}} = 0.02$ is also added. The evolution started from zero-age-main-sequence (ZAMS), and is terminated once the models reach $T_{\text{eff}} = 10000$ K after core hydrogen depletion. We stored equilibrium models for every ~ 0.001 drop in center hydrogen X_{c} during the MS phase, and by 100 K change in T_{eff} during post-MS phase. For every model, we used GYRE (Townsend & Teitler 2013, v.4.2) to compute non-adiabatic frequencies of radial ($\ell = 0$), dipole ($\ell = 1$) and quadrupole ($\ell = 2$) zonal modes ($m = 0$) in the

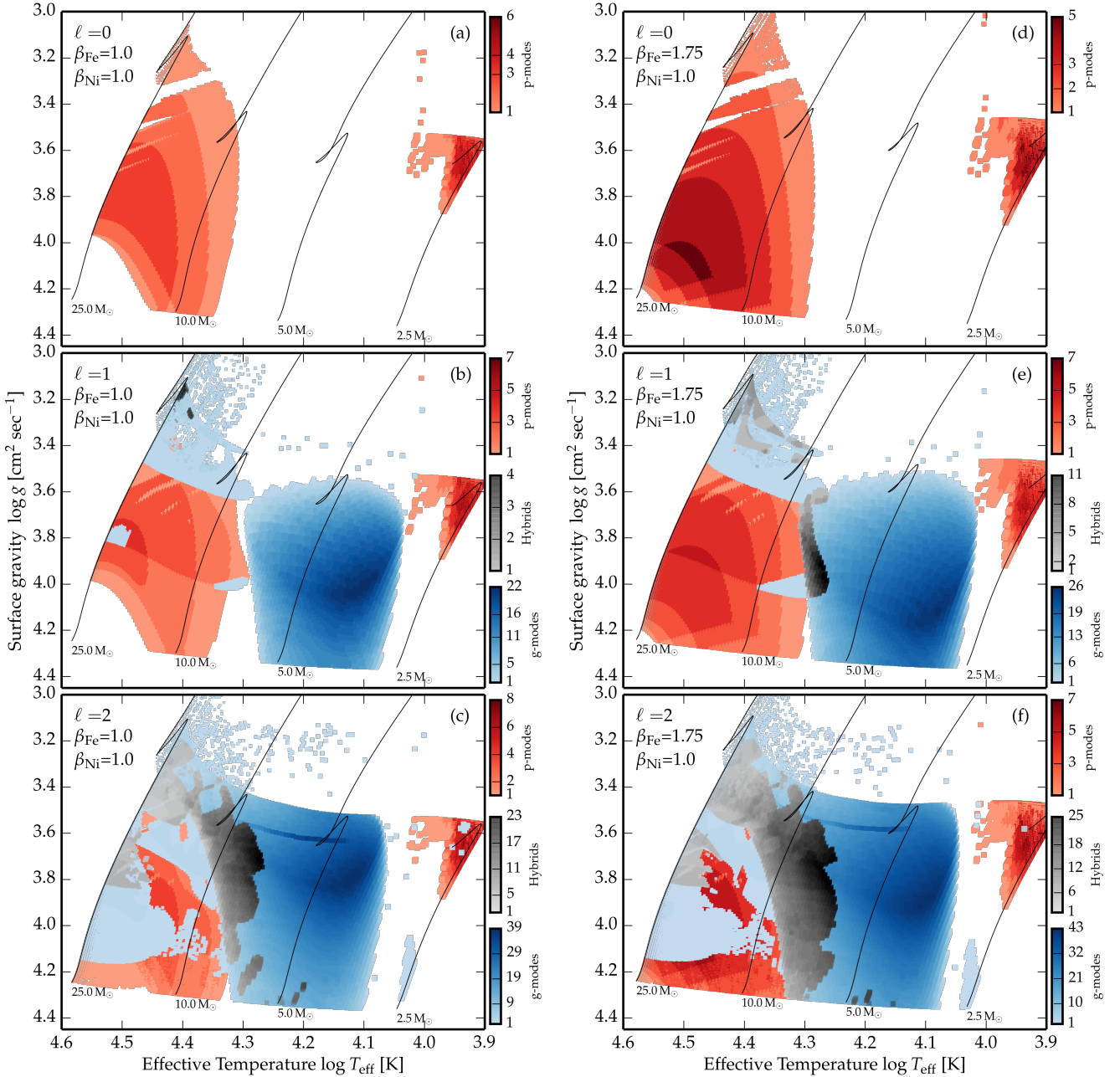


Figure 2. Instability strips of pure p-modes (red), pure g-modes (blue), and hybrid (grey) pulsators. Top, middle, and bottom panels show radial, dipole, and quadrupole modes, respectively. The left panels (a, b, c) correspond to tracks computed with $\beta_{\text{Fe}} = \beta_{\text{Ni}} = 1.0$, and similarly the right panels (d, e, f) correspond to $\beta_{\text{Fe}} = 1.75$ and $\beta_{\text{Ni}} = 1.0$. All evolutionary tracks are computed with fixed metallicity $Z = 0.014$, the [Asplund et al. \(2009\)](#) mixture, and exponential core overshooting $f_{\text{ov}} = 0.02$. Four tracks are shown for comparison. Tracks are computed only between 2.5 to 25 M_{\odot} . Colors encode the number of unstable modes. Refer to the color figure for better visibility.

frequency range 0.4 to 20 d^{-1} . We discriminate between p-modes ($n_{\text{pg}} \geq 0$) and g-modes ($n_{\text{pg}} < 0$) based on the net radial order $n_{\text{pg}} = n_{\text{p}} - n_{\text{g}}$; here, n_{p} (or n_{g}) is the number of p- (or g-) dominated radial nodes. The excited modes are distinguished by considering the sign of the imaginary part of the eigenfrequencies ([Unno et al. 1989](#)), and then enumerated. [Dziembowski & Pamyatnykh \(2008\)](#) define hybrid pulsators as those which exhibit β Cep variability simultaneously with SPB type. However, there is no clear-cut definition of low-order versus high-order modes in terms of n_{pg} , and one must set a definition. We identify a model as a hy-

brid, once it has at least one unstable low-order p- and/or g-mode ($-2 \leq n_{\text{pg}} \leq +2$), in addition to at least one unstable high-order g-mode ($n_{\text{pg}} < -3$). This allows classifying each model into being a pure p-mode, pure g-mode, or hybrid pulsator.

4 REVISED INSTABILITY STRIPS OF THE UPPER HR DIAGRAM

Fig. 2 shows the instability strips of the unstable radial (top), dipole (middle), and quadrupole (bottom) modes using $\beta_{\text{Fe}} = \beta_{\text{Ni}} = 1.0$ tables (left) and $\beta_{\text{Fe}} = 1.75, \beta_{\text{Ni}} = 1.0$ tables (right). The instability strip for $\beta_{\text{Fe}} = \beta_{\text{Ni}} = 1.75$ grid is quite similar to that of $\beta_{\text{Fe}} = 1.75$, and not shown here.

The immediate consequence of increasing β_{Fe} from 1.0 to 1.75 is an increase in the number of unstable g-modes and hybrids. In Fig. 2a there is a gap at higher mass near the ZAMS for $\log T_{\text{eff}} \gtrsim 4.45$, where no unstable modes are predicted (Pamyatnykh 1999; Saio 2011; Walczak et al. 2015). However, this region is filled up in Fig. 2d by few low-order radial modes thanks to $\beta_{\text{Fe}} = 1.75$. The same is true for dipole p-modes. Thus, all stars more massive than $\sim 7 M_{\odot}$ exhibit β Cep type variability as soon as they reach the ZAMS. In Fig. 2b, the SPB instability strip is separated from the β Cep strip, while in Fig. 2e the two regions smoothly merge, giving rise to a much extended hybrid instability domain. This is because the β Cep instability strip has now stretched to lower T_{eff} , and the SPB strip has extended to higher and lower T_{eff} . The quadrupole g-mode instability domain in Figs. 3c and 3f seems to be a common pulsation feature of all massive O- and B-type stars, and the role of Fe contribution to the opacity has a sizeable influence on the widening of the hybrid region towards lower effective temperatures and higher surface gravities.

The SPB instability strip hosts rich high-order dipole and quadrupole g-mode pulsators. The success of asteroseismic modelling of SPB stars (e.g. Moravveji et al. 2015) depends a priori on identifying consecutive series of g-modes with the same degree ℓ that form a period spacing, with a possible deviation from the asymptotic spacing. Such modes probe the extent, thermal and chemical structures of the overshooting layer on top of the convective core, in addition to the μ -gradient layer (Moravveji 2015). Thus, SPBs are promising asteroseismic targets for space observations, and should be carefully selected. The dark blue patches in Figs. 2b, 2c, 2e and 2f mark the position of most unstable g-modes with initial mass $\sim 3.5 M_{\odot}$. This clearly explains the recent discovery of the two *Kepler* SPB stars, namely KIC 10526294 ($\sim 3.25 M_{\odot}$, Pápics et al. 2014; Moravveji et al. 2015) and KIC 7760680 ($\sim 3.3 M_{\odot}$, Pápics et al. 2015), with 19 and 36 identified consecutive dipole g-modes, respectively. At higher surface gravities, such stars are first rich dipole pulsators, which later on, turn into rich quadrupole pulsators (Figs. 2e and 2f). Moreover, this richness explains the large number of observed significant low-frequency peaks in the g-mode frequency range in numerous additional *Kepler* SPB candidates yet to be analysed in full detail. The predicted position of the richest SPB stars (dark blue patches in Fig. 2) is a roadmap for selecting future targets for the on-going BRITE-constellation, the two-wheel *Kepler* (abbreviated K2), and the future PLATO space missions.

Below the SPB instability strip where the partial He ionization region destabilizes the high-order δ Scuti-type variability (Pamyatnykh 1999), we find unstable low-degree p-modes and quadrupole g-modes. Even though this is below our region of attention, but it is worth to mention that recently Balona et al. (2015) predicted that a factor 2 increase in the Fe opacity around $\log T \sim 5.06$ can destabilize

Table 1. List of confirmed SPB- β Cep pulsators. The given ID is the numbers used to mark each star in Fig. 3.

Star Name	ID	$\log T_{\text{eff}}$ [K]	$\log g$ [cm/sec ²]	Var. Type
HD 46202 ^(a)	1	4.533±0.005	4.18±0.05	β Cep
EPIC 202060092 ^(b)	2	4.544±0.050	4.50±0.50	β Cep
γ Peg ^(a)	1	4.325±0.026	4.15±0.15	Hybrid
ν Eri ^(a)	2	4.371±0.018	3.75±0.15	Hybrid
12 Lac ^(a)	3	4.389±0.017	3.65±0.15	Hybrid
16 Mon ^(c)	4	4.301±0.021	4.20±0.10	Hybrid
V1449 Aqu ^(a)	5	4.389±0.026	3.83±0.30	Hybrid
HD 50230 ^(a)	6	4.255±0.035	3.80±0.30	Hybrid
HD 43317 ^(d)	7	4.225±0.025	3.90±0.10	Hybrid
HD 170580 ^(e)	8	4.301±0.021	4.10±0.15	Hybrid

(a) Aerts (2013) and references therein, (b) Buysschaert et al. (2015): the star has a poorly known fundamental parameters due to its binary nature, poor quality spectra and inadequate orbital monitoring; thus, we assumed 2000 K uncertainty in T_{eff} and 0.5 dex in $\log g$, (c) Thoul et al. (2013), (d) Briquet et al. (2013): it is the only magnetic and rapid rotator (50% critical) here, and its position on the Kiel diagram is less secure, (e) CoRoT target (Conny Aerts, private communication).

g-modes and allows explaining the observed low-frequency peaks in their *Kepler* sample of A- and F-type δ Scuti pulsators. Thus, our results agrees with their predictions, too.

5 OBSERVED AND PREDICTED DOMAINS OF HYBRID PULSATORS

To manifest the consistency of the enhanced Fe opacity with the observed instability domains of heat-driven massive pulsators, we make two comparisons between the observed position of two confirmed late O-type β Cep pulsators, and all confirmed SPB- β Cep hybrids from the literature. Table 1 gives a summary of these carefully selected targets.

Fig. 3 shows the instability region of dipole p-modes (left), and hybrids (right) from the three ($\beta_{\text{Fe}}, \beta_{\text{Ni}}$) combinations of (1.0, 1.0) in light grey, (1.75, 1.0) in medium grey, and (1.75, 1.75) in dark grey. In Fig. 3a, an increase in β_{Fe} (and to lesser extent β_{Ni}) extends the instability domain of pure dipole p-modes, and fills up the gap at the high temperature and surface gravity region up to the ZAMS. This explains the presence of the only two observed β Cep pulsators in this gap, which were formerly unexplained. Unfortunately, there exists no more confirmed late O-type β Cep stars in this extreme region, and future K2, BRITE-constellation and PLATO observations can hopefully improve the picture. In Fig. 3b, the Fe opacity enhancement unambiguously extends the hybrid instability domain by ~ 0.2 dex to higher surface gravities, and by ~ 0.1 dex to lower T_{eff} . Thus, the eight SPB- β Cep hybrids either fall inside the hybrid domain, or are much closer to the boundary compared to the case $\beta_{\text{Fe}} = 1.0$. As an example, Fig. A1 demonstrates how unstable modes can be destabilized by increasing β_{Fe} and β_{Ni} for the first three hybrids in Table 1.

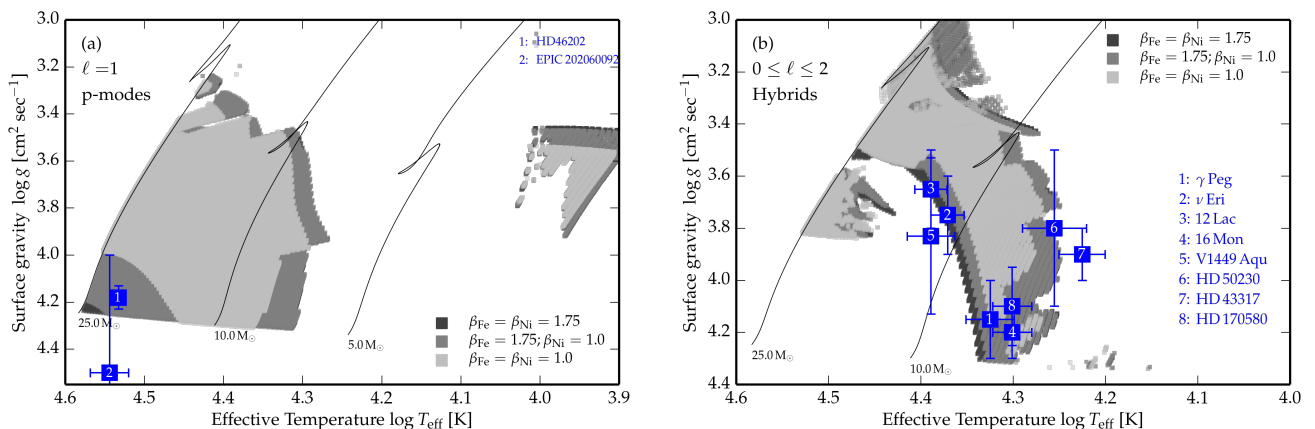


Figure 3. The extension of dipole p-mode (left) and low-degree hybrid instability strips for massive OB-type stars on the Kiel diagram. The light grey corresponds to $(\beta_{\text{Fe}}, \beta_{\text{Ni}})=(1.0, 1.0)$, the medium grey corresponds to $(1.75, 1.0)$ and the dark grey corresponds to $(1.75, 1.75)$. Clearly, Ni opacity enhancement has minute impact on extending the instability domains in both cases. The blue squares show the position of confirmed β Cep (left) and hybrid pulsators (right). Table 1 gives an overview of these targets.

6 CONCLUSIONS

The long-standing difficulty to destabilize heat-driven modes that were present in the observations but not predicted in theory can be accurately resolved by enhancing the Iron opacity by $\sim 75\%$ in the models. This factor comes from direct opacity measurement of Bailey et al., and better explains the distribution of ten β Cep and hybrid pulsators on the Kiel diagram. The required increase in the Z-bump was correctly predicted by many authors such as Dziembowski & Pamyatnykh (2008) for ν Eri (Table 1) and Salmon et al. (2012) for the LMC variables. Thus, *the input physics of stellar models should now adapt to $\beta_{\text{Fe}} = 1.75$* and consider more opaque stellar plasma, to provide a more realistic picture of massive stellar structure, evolution, and pulsation.

During the evolution of SPBs, the number of excited modes evolves as well. This flags late B-type stars of $\sim 3M_{\odot}$ to $4M_{\odot}$ as the most promising asteroseismic targets for the on-going space based photometry by the K2, and BRITE-constellation, in addition to the future PLATO missions. Such observations will deliver input to distinguish between different types of observed variability in OB-type stars, such as rotational modulation, excitation by κ -mechanism, stochastic excitation of p-modes (Degroote et al. 2010), and excitation by internal gravity waves (Aerts & Rogers 2015).

ACKNOWLEDGEMENTS

E. Moravveji thanks Conny Aerts (KU Leuven) and Cole Johnston (KU Leuven) for reading the manuscript, and is grateful to Haili Hu (SRON), Aaron Dotter (ANU), Peter Pápics (KU Leuven), Bill Paxton (UCSB), and Geert Jan Bex (UHasselt) for valuable discussions and support. The research leading to these results has received funding from the People Programme (Marie Curie Actions) of the European Union’s Seventh Framework Programme FP7/2007-2013/ under REA grant agreement n° 623303 for the project ASAMBA. The computational resources and services used in this work were provided by the VSC (Flemish Supercomputer Center), funded by the Hercules Foundation and the Flemish Government - department EWI.

REFERENCES

- Aerts C., 2013, in EAS Publications Series. pp 323–330
- Aerts C., Rogers T. M., 2015, *ApJ*, **806**, L33
- Asplund M., Grevesse N., Sauval A. J., Scott P., 2009, *ARA&A*, **47**, 481
- Badnell N. R., Bautista M. A., Butler K., Delahaye F., Mendoza C., Palmeri P., Zeppen C. J., Seaton M. J., 2005, *MNRAS*, **360**, 458
- Bailey J. E., et al., 2015, *Nature*, 517, 56
- Balona L. A., Daszyńska-Daszkiewicz J., Pamyatnykh A. A., 2015, *MNRAS*, **452**, 3073
- Briquet M., Neiner C., Leroy B., Pápics P. I., 2013, *A&A*, **557**, L16
- Buysschaert B., et al., 2015, *MNRAS*, **453**, 89
- Degroote P., et al., 2010, *A&A*, **519**, A38
- Dziembowski W. A., Pamyatnykh A. A., 1993, *MNRAS*, **262**, 204
- Dziembowski W. A., Pamyatnykh A. A., 2008, *MNRAS*, **385**, 2061
- Dziembowski W. A., Moskalik P., Pamyatnykh A. A., 1993, *MNRAS*, **265**, 588
- Gautschi A., Saio H., 1993, *MNRAS*, **262**, 213
- Godart M., Noels A., Dupret M.-A., Lebreton Y., 2009, *MNRAS*, **396**, 1833
- Hu H., Glebbeek E., Thoul A. A., Dupret M.-A., Stancliffe R. J., Nelemans G., Aerts C., 2010, *A&A*, **511**, A87
- Iglesias C. A., 2015, *MNRAS*, **450**, 2
- Moravveji E., 2015, preprint, ([arXiv:1508.00813](https://arxiv.org/abs/1508.00813))
- Moravveji E., Aerts C., Pápics P. I., Triana S. A., Vandoren B., 2015, *A&A*, **580**, A27
- Nieva M.-F., Przybilla N., 2012, *A&A*, **539**, A143
- Pamyatnykh A. A., 1999, *Acta Astron.*, **49**, 119
- Pápics P. I., Moravveji E., Aerts C., Tkachenko A., Triana S. A., Bloemen S., Southworth J., 2014, *A&A*, **570**, A8
- Pápics P. I., Tkachenko A., Aerts C., Van Reeth T., De Smedt K., Hillen M., Østensen R., Moravveji E., 2015, *ApJ*, **803**, L25
- Paxton B., Bildsten L., Dotter A., Herwig F., Lesaffre P., Timmes F., 2011, *ApJS*, **192**, 3
- Paxton B., et al., 2013, *ApJS*, **208**, 4
- Paxton B., et al., 2015, preprint, ([arXiv:1506.03146](https://arxiv.org/abs/1506.03146))
- Saio H., 2011, *MNRAS*, **412**, 1814
- Salmon S., Montalbán J., Morel T., Miglio A., Dupret M.-A., Noels A., 2012, *MNRAS*, **422**, 3460
- Seaton M. J., 2005, *MNRAS*, **362**, L1
- Seaton M. J., Yan Y., Mihalas D., Pradhan A. K., 1994, *MNRAS*, **266**, 805

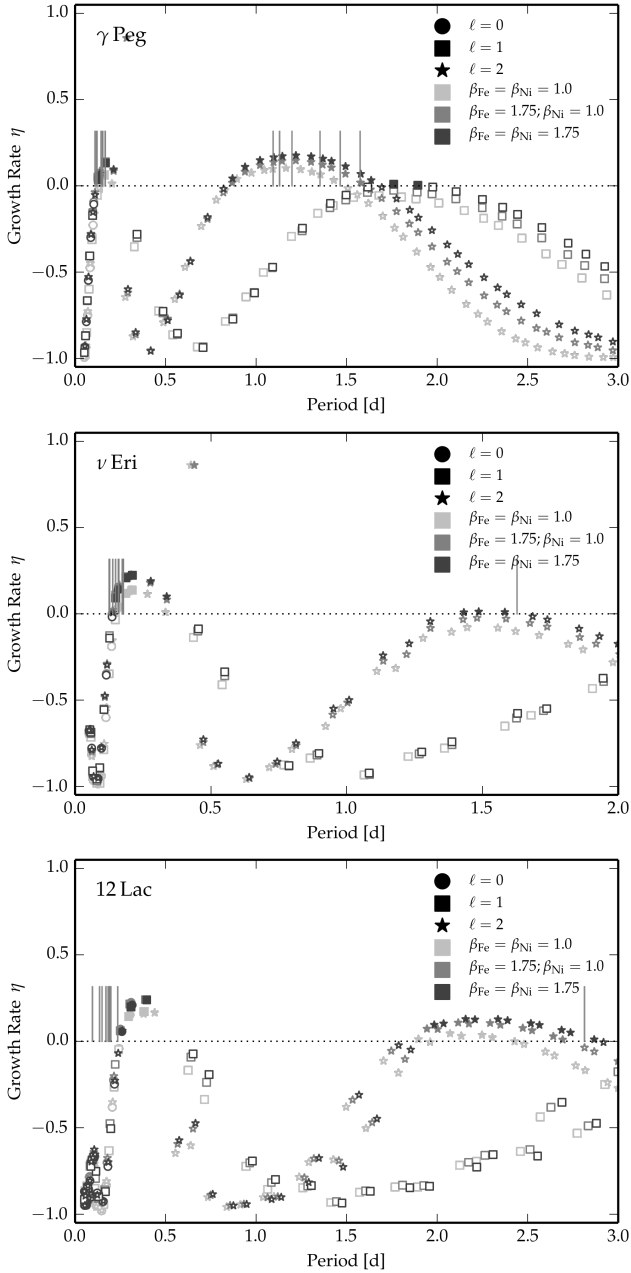


Figure A1. Theoretical growth rate η for γ Peg (top), ν Eri (middle) and 12 Lac (bottom). For each object, the input models are close to their spectroscopic T_{eff} and $\log g$ (see Table 1). The vertical lines mark the observed period of each star.

Thoul A., et al., 2013, *A&A*, 551, A12

Townsend R. H. D., Teitler S. A., 2013, *MNRAS*, 435, 3406

Unno W., Osaki Y., Ando H., Saio H., Shibahashi H., 1989, Non-radial oscillations of stars

Walczak P., Fontes C., Colgan J., Kilcrease D. P., Guzik J. A., 2015, *A&A*, 580, L9

APPENDIX A: GROWTH RATES

The normalized growth rate $\eta = W / \int_0^{R_*} |dW/dr| dr$ predicts if a mode is stable ($W \leq 0$) or unstable ($W > 0$) against destabi-

lizing effect of the κ -mechanism. W and dW/dr are the net and differential work, respectively (Unno et al. 1989). Increasing β_{Fe} and β_{Ni} is expected to destabilize the marginally stable modes, give rise to larger number of excited modes, and consequently extend the instability domains. We take the first three stars from Table 1, and select three representative models for each star from our grids close to their position on the Kiel diagram. The initial mass of these models agree with the literature. The growth rates are shown in Fig. A1. For ν Eri and 12 Lac, the more opaque models can better explain their high-order g-mode. Note that the exact reproduction of the observed frequencies of each star is beyond the purpose of this Letter; we only intend to show that the enhanced Fe and Ni opacities can better explain the number of observed modes in these hybrid pulsators, specifically their high-order g-modes.

This paper has been typeset from a $\text{\TeX}/\text{\LaTeX}$ file prepared by the author.